Journal of Materials Chemistry A

Accepted Manuscript

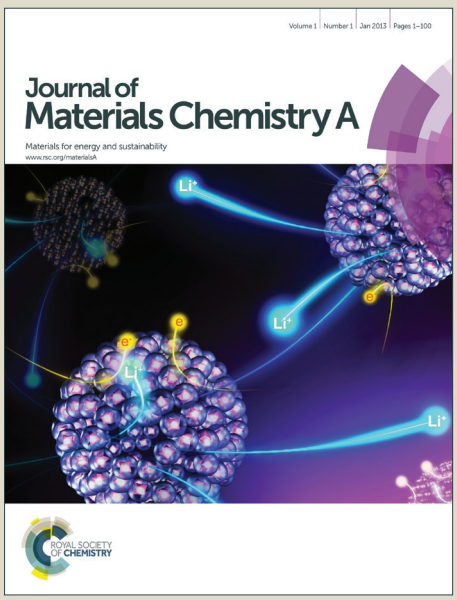

ROYAL SOCIETY OF CHEMISTRY

www.rsc.org/materialsA

Deformable fibrous carbon supported ultrafine nano-SnO_2 as a high volumetric capacity and cyclic durable anode for Li storage

Renzong Hu[1,2], Hanyin Zhang[1], Jiangwen Liu[1], Dongchang Chen[2], Lichun Yang[1], Min Zhu[1], and Meilin Liu[2]**

[1]Guangdong Provincial Key Laboratory of Advanced Energy Storage Materials, School of Materials Science and Engineering, South China University of Technology, Guangzhou, 510640, China
E-mail: memzhu@scut.edu.cn

[2] School of Materials Science and Engineering, Georgia Institute of Technology, Atlanta, GA 30332-0245, US
E-mail: meilin.liu@mse.gatech.edu

Keywords: lithium ion battery, deformable fibrous carbon, tin dioxide, stress release, *in*-situ Raman spectrum

Abstract:

Multidimensional fibrous carbon scaffolds, derived from carbonized filter papers (CFP), was used to support SnO2 nanocrystals (NC, with size of 4~5nm) to form a free-standing SnO2NC@CFP hybrid anode for Li-ion batteries. The SnO_2NC particles are well accreted on the surfaces of 1D carbon fibers and 2D ultrathin carbon sheets while maintaining 3D interconnected pores of the carbon matrices for fast ionic transport. The SnO_2NC@CFP hybrid electrode exhibits long-term higher energy density than the commercial graphite anode, and excellent rate capability, due mainly to good dispersion of SnO_2 in the multidimensional conductive carbon. In particular, the reversible deformation of the flexible fibrous carbon matrices, as inferred from *in* situ Raman spectroscopy and SEM image analysis, facilitates stress release from the active SnO_2NC during discharge-charge cycling while maintaining structure integrity of the self-supported SnO_2NC@CFP anode. These demonstrate that rational combination of multidimensional architecture of deformable carbon with nanoscale active materials is ideally suited for high-performance Li–ion batteries.

1. Introduction

To meet the power demands of many emerging applications such as electric vehicles and smart grids, it is necessary to significantly increase the capacity/energy densities and prolong the lifespan of the existing lithium ion batteries (LIBs); this is a great challenge to the battery industries and the scientific communities[1]. To overcome this challenge, various intriguing designs and strategies have been proposed for dramatically enhancing the performance of the electrodes [2]. As one of the most promising alternative anode materials, tin dioxide (SnO_2) has attracted much attention due to its high theoretical capacities and moderate operating potential for Li storage in comparison to graphite and other transition metal oxides[3-10]. It is well known that SnO_2 stores Li^+ by a two-step process, a conversion reaction ($SnO_2+Li^+ \longleftrightarrow Sn+Li_2O$) followed by an alloying reaction ($Sn + xLi^+ \longleftrightarrow Li_xSn$), corresponding to a theoretical capacity of 711 and 783 $mAhg^{-1}$, respectively [5, 11]. Thus, the theoretical capacity (1,494 $mAhg^{-1}$) is about four times of that of graphite (372 $mAhg^{-1}$). However, severe capacity fading during cycling is still the greatest challenge for SnO_2 anode to be commercially viable, due mainly to disintegration of the electrode structure resulted from the huge volume change and serious aggregation of Sn particles during the alloying reaction[5, 12], as well as poor electron/ion conductivity of the oxides. Further, SnO_2 based anodes have large initial capacity loss, due primarily to the irreversibility of Li_2O in the conversion reaction, in addition to other Li-consuming irreversible reactions on new surfaces of electrodes[6, 13, 14]. Accordingly, nanoparticles of SnO_2 have been integrated with different forms of carbonaceous (C) matrices [15-24] to enhance the structural stability and reaction reversibility of SnO_2 anodes.

The function of the carbonaceous additives in a SnO_2-C hybrid electrode is twofold; it may act as a matrix to buffer the volume change of SnO_2 and to enhance the conductivity of the electrode. However, the specific morphology and architecture of the carbon supports dramatically affect the performance of the hybrid electrode [25-28]. 1D carbon structures (e.g.,

nanowire, nanotube, and electrospun microfiber) could achieve fast Li^+ transport kinetics in one direction, but offer low loading of SnO_2 and thus low electrode capacity due to small surface areas [20, 29-31]. For 2D carbon matrices with higher surface areas (such as grahene, ultrathin carbon sheets, and carbon coating), more SnO_2 particles could be loaded with good electrical contact, resulting in higher capacity and enhanced cycleability[28, 32-34]. However, large initial irreversible capacity loss was inevitable due to the high surface areas of the hybrids [35]. In contrast, 3D interconnected carbon structures (e.g., porous carbon, fiber networks, and fiber papers) with continuous transport pathways allow fast Li^+/e^- transport in any dimensions while maintaining a superior structural integrity for the SnO_2[36-38]. Nevertheless, the volumetric capacity of the 3D porous hybrids is relatively low due to the large-sized pores of the carbon skeletons. Furthermore, it was found that Li_2O may be partly decomposed, yielding higher reversible capacity if ultrafine SnO_2 particles were well combined with nanosized carbon [28, 39]. Accordingly, new electrode architectures are required to mitigate the problems associated with the existing hybrid electrodes. An effective approach could be a rational combination of multidimensional (1D, 2D, 3D) carbon with well-dispersed nanoisized SnO_2 phases.

It is found in a previous study that the deformability (or superelasticity) of a supporting matrix is vital to effectively accommodating the volume change of Sn-based active materials during Li^+ insertion and extraction[40]. Accordingly, a deformable carbon frame may help to suppress the volume expansion effect of lithiated SnO_2. Here we demonstrates the rational design of a multidimensional SnO_2-C hybrid electrode by simply using carbonized filter paper (CFP), which has a 3D porous structure consisting of 1D micro /nanosized carbon fibers and 2D ultrathin carbon sheets. The electrode was prepared by electrodepositing SnO_2 nanocrystals (NC) on CFP, which was different strategy to those previously reported work that usually using filter papers as templates to form SnO_2–C nanofibers[41, 42]. This unique SnO_2NC@CFP hybrid electrode was used as a self-supporting anode excluded the additional

binder and current collectors, in which the carbon scaffolds were deformable and flexible to release the stress induced by lithiation of SnO_2, displaying high gravimetric and volumetric capacity, excellent rate capability and long cycling life.

2. Experimental Sections

Fabrication of porous carbonized filter papers (CFP): The commercial filter paper sheets (Hang Zhou Filter paper Co. Ltd) were placed in an alumina boat in a horizontal tube furnace, and carbonized at 450℃ for 4 hour as a H_2/Ar gas mixture (92%Ar+8%H_2) was flowed through the tube to form black CFP sheets.

Electrodeposition of SnO_2 nanocrystals on CFP sheets (SnO_2NC@CFP): The solution (250mL) for electro-deposition was composed of 20 mM tin dichloride ($SnCl_4$, 99.8%), 100 mM sodium nitrate ($NaNO_3$, ~99%), 75 mM nitric acid (HNO_3), and distilled water. A rectangle piece of CFP (1×1.5cm) was used as the working electrode, which was soaked in the above solution for 2h before electrodeposition. A conventional three-electrode cell was used for the electro-deposition in which a platinum (Pt) metal plate was used as the counter electrode with a separation from the working electrode by 2 cm. A saturated calomel electrode (SCE) was used as the reference electrode. SnO_2 were deposited using a potentiostat (CHI600E, China) with working potential of -0.2V (vs. SCE). The SnO_2 loading in CFP matrix was dependant on the depositing time and the concentration of Sn-based solution. However, It was also found that the morphology in different samples were dramatically different. Duration of 30 min for electrodeposition had been chosen after optimization. The deposits were washed with water and then immersed in deionized water to leach the remaining chloride impurity. The specimens were dried at 200 °C for 4h in a drum wind drying oven, and finally the brown self-supporting SnO_2NC@CFP hybrids were obtained. Pure SnO_2NC powders (with average crystal size 4-5nm, see Figure S5, Supporting Information) formed during the deposition, in the solution near under the working electrodes, were also collected and dried at 200 °C for 4h in a drum wind drying oven.

Synthesis of a physical mixture of pure SnO_2NC powders and CFP (SnO_2NC+CFP mixture): 20mg SnO_2NC powders and 30mg CFP powders were put together in an agate mortar, and then grinded by hand for 30 min to form a mixture of SnO_2NC and CFP.

Materials characterization: The morphologies of the samples were characterized using a Carl Zeiss Supra 40 field emission scanning electron microscope (SEM) and a JEOL JEM-2100 transmission electron microscope (TEM) operating at 200kV. The phase variations of the samples were determined using a Philips X-ray diffractometer (XRD) with Cu-Kα radiation and a Raman spectrometer (Raman, Horiba) with a 632.81nm excitation laser. The electronic states of O in the electrodes were determined by an AXIS Ultra DLD X-ray photoelectron spectrometer (XPS) using Al-K_α radiation. Raman spectra were obtained using a Renishaw RM 1000 spectromicroscopy system with an air-cooled Ar laser emmited 446nm. Thermogravimetric (TG) analysis was performed under O_2 on NETZSCH STA409 with a heat rate of 10℃/min.

Electrochemical measurements: The discharge–charge cycling performance of the samples was investigated using a cell test system (LAND-CT2001A) with CR2016 coin-type cells, while the specific capacities of all reported composites were calculated from their total mass. The binder-free CFP (1cm ×1cm, ~ 4 mg), SnO_2NC@CFP sheets (1cm ×1cm, ~6.5mg), and commercial graphite anode coated on Cu foil (MTI Cooperation) were directly used as the working electrodes. For the SnO_2NC electrode slurry-coated on Cu foil substrates, it was consisted of 80 wt% of the active material, 10 wt% conductivity additives (Super-P), and 10 wt% binder polyvinyldifluoride. Lithium foil was used both as counter electrode and as reference electrode in the half cells. The electrolyte was $LiPF_6$ (1 mol/L) in a mixture of ethylene carbonate (EC)/diethyl carbonate (DEC)/ethyl methyl carbonate (EMC) with a volume ratio of EC/DEC/EMC=1:1:1 (Shanshan Tech Co., Ltd.). The cells were tested at various current rates between 0.01 and 2.0 V at room temperature. For *in*-situ Raman observation, the SnO_2NC@CFP and pristine CFP sheets were acted as the working electrodes

in a spectroelectrochemical cell (MTI Cooperation). A small hole was made in the lithium foil and separator in order to observe the electrode surface. The electrolyte mixture of 1M LiBOB in PC was used in the *in*-situ Raman cells due to the serious fluorescence effects of $LiPF_6$ weaken the Raman signal of carbon and SnO_2. The *in*-situ Raman cell was galvanostatically tested using a Solatron Analytical 1470E potentiostat. At the same time, an *in*-situ time-resolved study was conducted by placing the laser spot on the same location, with the laser slightly out of focus to cover a larger area of about 5μm in diameter.

3. Results and Discussion

It is well known that the filter papers (FP, actually the cellulose) possess porous network structure with complicated hierarchical morphology. The carbonization of FP in N_2 had been previously reported[43], but the final carbon paper was dense and without fibrous morphology, owing to the coalescence effect of the carbon species formed during the carbonization process of cellulose. In this study, we carbonized commercial FP sheets differently, in a rapid flow of a H_2/Ar mixture rather than in N_2. The surface hydroxyl groups could be quickly removed from cellulose to avoid coalescence of carbon under a reducing atmosphere H_2. Thus, the rapid H_2/Ar flow helped to maintain 3D porous structure in CFP. Furthermore, the rapid H_2/Ar flow could also help to thin the fibers and create pores in the carbon scaffolds (see detailed microstructure observation below and **Figure S1**, **Supporting Information**). In the preparation of hybrid anode, the CFP sheets were first immersed in an acidic electrolyte solution (with $SnCl_4$, $NaNO_3$ and HNO_3) for 2h to allow the solution to fully fill inside the pore space of the CFP due to the capillary force. During 30 minutes electrodepositing, $Sn(OH)_4$ formed and precipitated inside the pores and on surfaces of the CFP because of its low solubility. Finally, the $Sn(OH)_4$ was dehydrated at 200◦C to form SnO_2 nanocrystals in the CFP to yield a SnO_2NC@CFP hybrid. The hybrid contained ca. 39wt% of SnO_2 as determined from thermogravimetric (TG) analysis (**Figure S2, Supporting Information**).

The resultant SnO_2NC@CFP hybrid sheets possessed morphological characteristics of

the original CFP except for a little change in shape due to stress induced by SnO_2 deposition. As shown in the right top inset of **Figure 1a**, the SnO_2NC@CFP hybrid sheets were self-supporting with a thickness of ~110μm (see in Figure 6 later). Analysis of the XRD patterns of CFP, SnO_2NC powder, and SnO_2NC@CFP hybrid, as seen in Figure 1a, suggests that carbon in the CFP was amorphous before and after electrodeposition. The weak and broad peaks at 26.5°, 33.7° and 51.6° are an indication of the nanocrystalline nature of SnO_2 in both the pure SnO_2NC and hybrid sheet. XPS analysis also revealed the existence of Sn (14.5at %) in hybrid and increase of oxygen from 13.9at % for CFP to 39.1at % for the hybrid (Figure S3 and Table S1, Supporting Information).

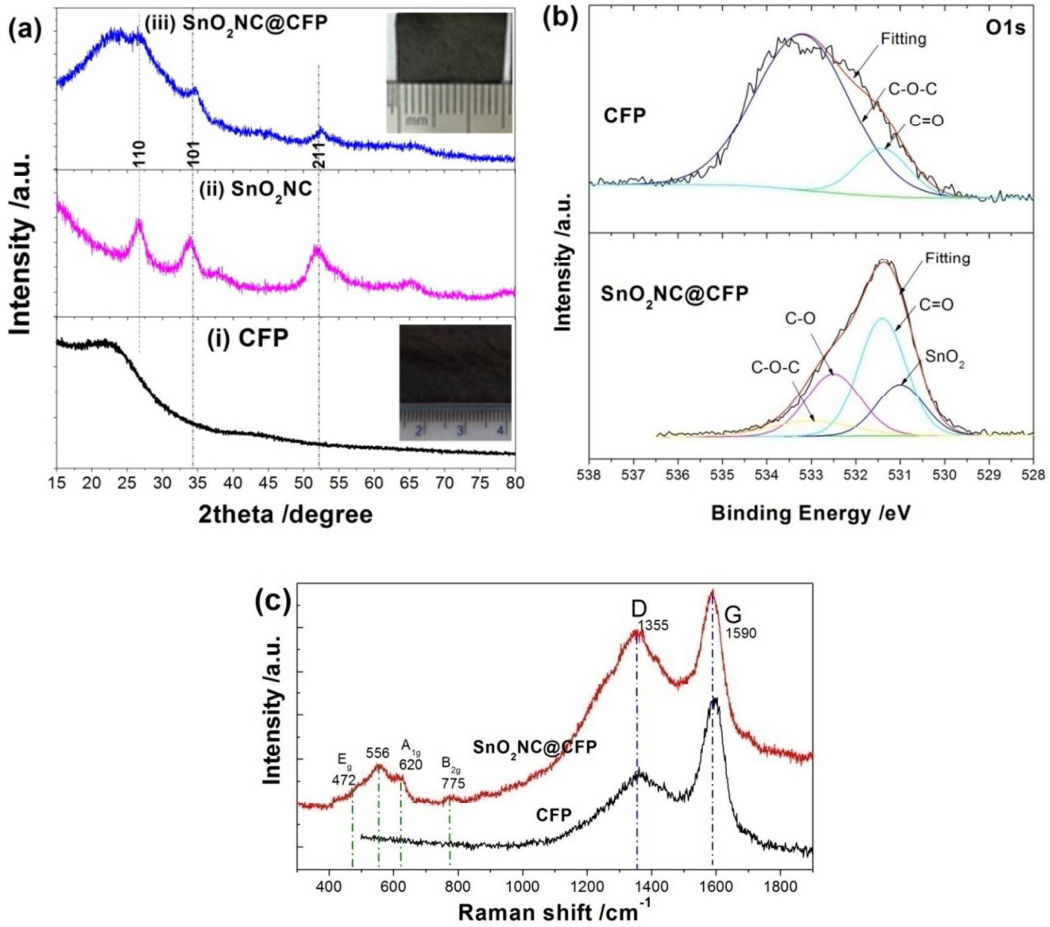

Figure1. (a) XRD patterns of (i) CFP bulk material, (ii) pure SnO_2 nanocrystals collected from precipitation near the working electrodes, and (iii) binder-free SnO_2NC@CFP; the insets are the images for CFP (lower right) and SnO_2NC@CFP sheets (top right), respectively; (b) O1s XPS spectra of CFP and SnO_2NC@CFP sheets. (c) Raman shits for the self-supporting CFP before and after depositing of SnO_2NC.

Additionally, as shown in **Figure 1b**, the O1s spectra suggested a dramatic increase of C-O and C=O bonding in the SnO_2NC@CFP hybrid in comparison with the CFP, which should be generated from the interface between SnO_2 and the carbon matrix. These interfaces were expected to enhance the bonding between SnO_2 and carbon in CFP. The C-O bonding should be generated from the interface between SnO_2 and the carbon matrix, which were expected to enhance the bonding between SnO_2 and carbon in CFP. However, the increase in C=O bonding should be attributed to the residual cellulose inside the fibers, which was exposed through the cracks formed in fibers during SnO_2 deposition and the subsequent heat-treatment in Air. It could be seen from the change in Raman features shown in **Figure 1c** that, after the deposition of SnO_2 on CFP, the intensity ratio of the D band to G band of carbon (I_D / I_G) increased to 0.81 from 0.53 for the pristine CFP, implying a change in the structure of the carbon[44]. Thus, the deposition of SnO_2 may lead to deformation and /or surface defects in the multidimensional carbon scaffolds. The C-O bonding at the interface between SnO_2 and carbon may also contribute to the increased I_D / I_G ratio. In addition, the E_g, A_{1g}, and B_{2g} band for crystalline SnO_2 are clearly seen at 472, 620 and 775cm^{-1}, respectively, in the Raman spectrum of the hybrid electrode while an obvious peak at around 556 cm^{-1} is attributed to amorphous SnO_2, [45] suggesting that a mixture of nano-crystalline and amorphous SnO_2 was formed on the CFP.

Figure 2a displays a typical SEM image for the CFP bulk material (inset in low right corner in **Figure.1a**). It clearly revealed the interconnected 3D porous structure (large amount of microsized holes and free-spaces) of the CFP, which consisted of random arrangement of the microsized fibrous carbon. As seen in the SEM images shown in **Figure 2b** and **c**, there were many 2D ultrathin carbon sheets (**Figure 2b** and **Figure S1,** Supporting Information) covered on the fibers, while micro-fibers were rolled up to form hollow tubes /grooves (**Figure 2c**). The 1D micro/nanofibers and the interconneted porous structure of the interlayer

of the CFP, as well as their amorphous nature were also identified by TEM observations (Figure S1, Supporting Information). These confirmed that the hierarchical structure of the initial FP was maintained, in addition to the multidimensional architecture after treating under a reducing Ar/H_2 atmosphere. It should be noted that this unique structure of CFP is quite different from the previously reported carbonized filter paper treated in nitrogen [43]. However, more controlled experiments need to be carried out to further study their formation processes. **Figure 2d** reveals the SEM image of the resultant SnO_2NC@CFP hybrid bulk sheets. It is clearly shown that the SnO_2 deposits were dispersed on the CFP while the 3D porous network and fibrous structure were maintained. Also, the higher magnification SEM images indicated that all the surfaces of the micro/nano-fibers (**Figure 2e** and **f**) as well as the ultrathin carbon sheets (**Figure 2g**) were completely accreted with ultrafine and uniform SnO_2 particles. Furthermore, careful examination of the hybrid suggests that the microfiber bundles were divided to nano-fibers (**Figure 2e**, and **Figure S4, Supporting Information**), resulted likely from the release of large stresses induced by SnO_2 growth on the surface of CFP.

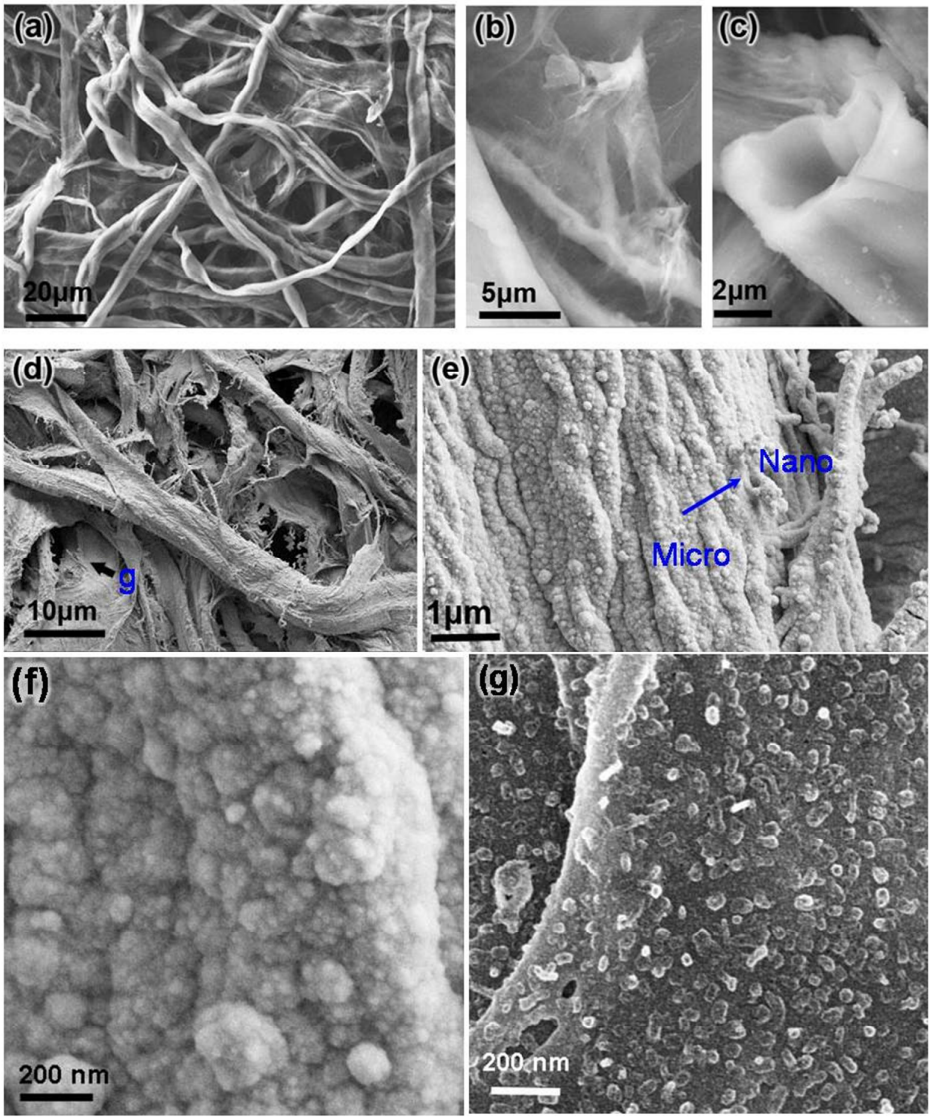

Figure 2 (a) SEM images of 3D porous CFP yielded by calcinations of commercial filter paper under a Ar/H_2 atmosphere; (b) and (c) large magnification SEM images reveal the existence of 2D ultrathin carbon sheets and hollow tubes;(d) typical SEM image of the as-prepared SnO_2NC@CFP sheet; (e) and (f) higher magnification SEM images showing the surface morphology of micro-size fibers after depositing of SnO_2NC; (g) Enlarged SEM image for zone arrowed in (d), showing the coverage of ultrafine SnO_2 particles on the 2D ultrathin carbon sheets.

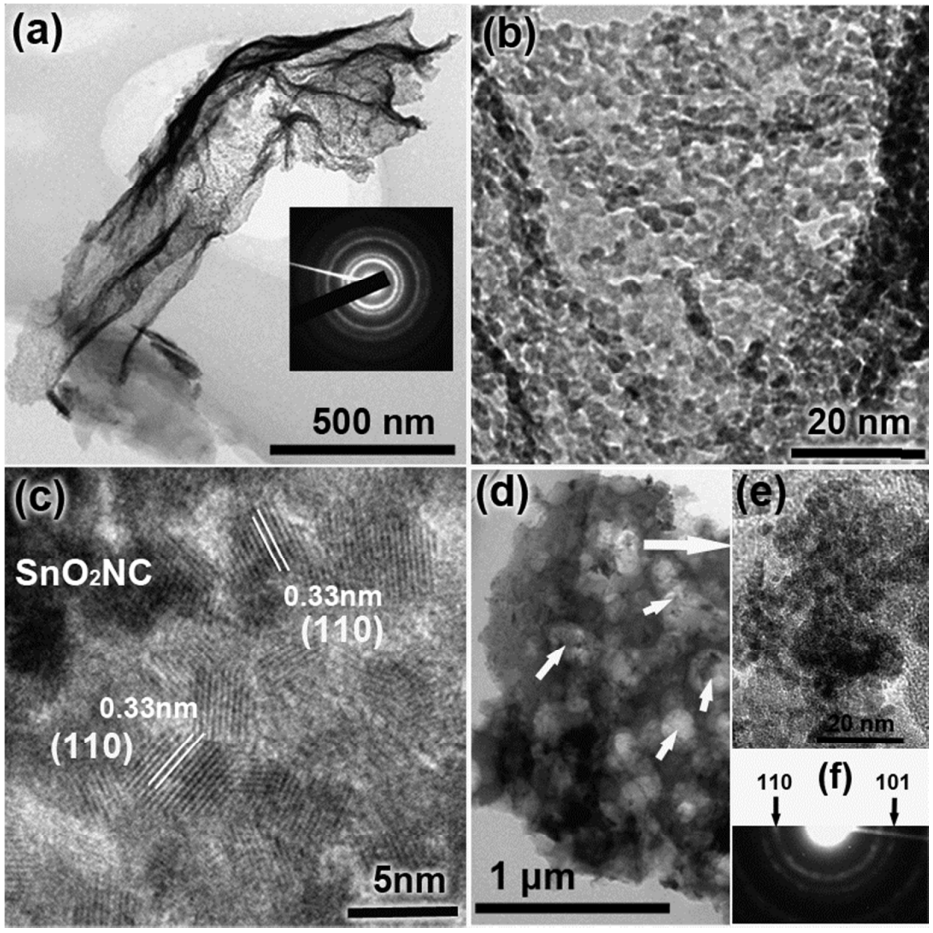

Figure 3 (a) TEM images for the 2D ultrathin carbon sheets in the SnO_2NC@CFP hybrid, insert: the corresponding SAED pattern; (b) enlarge image, and (c) HRTEM image for the zone arrowed in (b); (d) TEM image for the inner porous layer of the hybrid, arrows indicated the deposits in pores; (e) and (f) enlarge TEM image and its SAED pattern for zone arrowed in (d).

The TEM image of the SnO_2NC@CFP hybrid (**Figure 3a**) clearly shows the variation of the 2D ultrathin carbon sheets in the CFP after SnO_2 loading and the heat treatment. The continuous rings in the selected-area electron diffraction (SAED) pattern (**inset of Figure 3a**) further confirmed the presence of polycrystalline SnO_2. Enlarged TEM and HRTEM images (**Figure 3b** and **c**) revealed that uniform SnO_2 nanocrystals (4-5nm) were homogeneously distributed in the ultrathin carbon sheets. High dispersion state of ultrafine SnO_2 on micro/nano-fibers in the SnO_2NC@CFP hybrid was also observed, in comparison with the pure SnO_2NC (**Figure S4** and **S5,** Supporting Information). TEM image in **Figure 3d**

indicated that the inner layer of the CFP remained the porous structure in the electrodeposited hybrid, whereas most of the micro-pores were also filled with deposits (indicated by arrows). However, it was found that most of the deposits were aggregated in the pores rather than dispersed on their inner surfaces (**Figure S4, Supporting Information**). Enlarged image in **Figure 3e** showed that the aggregations were also ultrafine SnO_2 nanocrystals, with distinguishable (110) and (101) diffraction rings as indicated in **Figure 3f**, while the pores had free-space to accommodate the volume variation of these nanosized SnO_2 aggregates.

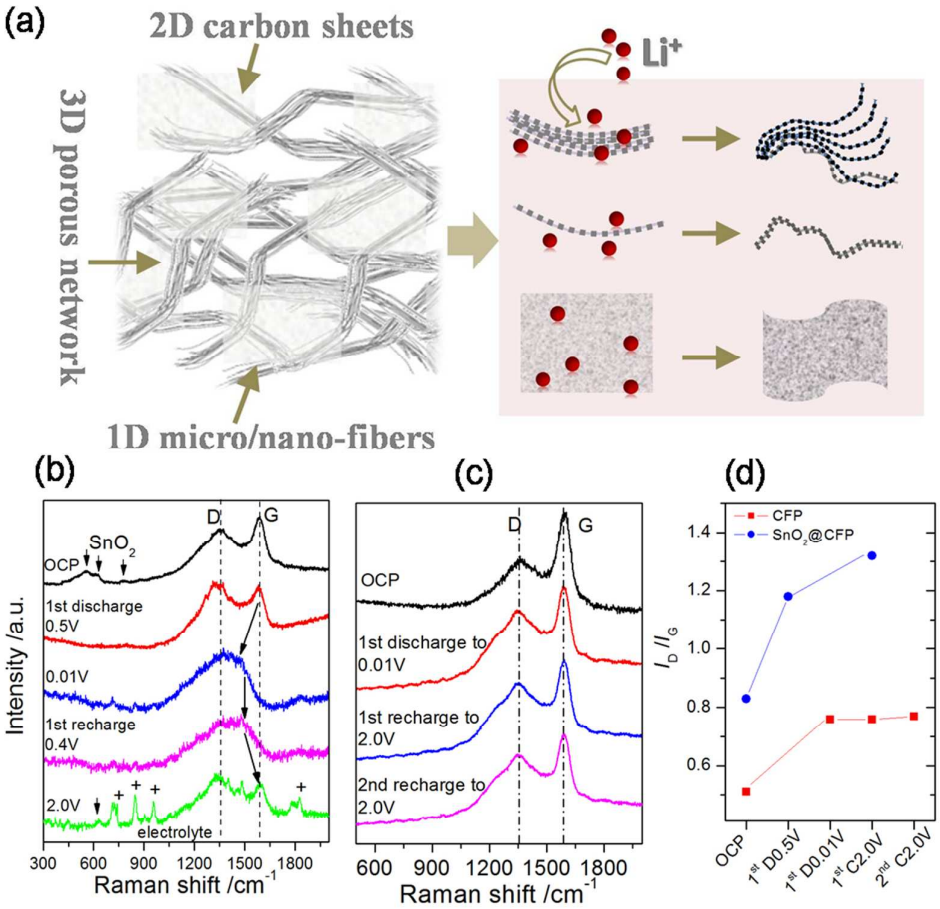

Figure 4 (a) Illustration for the flexibility (shape variation) of the multidimensional fibrous carbon, induced by the stress resulted from volume expansion of SnO_2 during reacting with Li. The 1D nanofibers and 2D carbon sheets could be bendable, while the microfibers were expected to split to be flexible nanofibers, to maintain the integration of SnO_2 layers. (b) *In*-situ Raman spectrum of the SnO2@CFP electrode collected at different lithiation state for the 1st cycle. (c) *In*-situ Raman spectrum of the CFP electrode collected at different lithiation state for the first two cycles. (d) Comparison the I_D/I_G of the CFP and SnO_2@CFP at different potential states.

Based on the above observations, our designed concept, i.e., the multidimensional configuration and interconnected porous structure of the SnO_2NC@CFP self-supporting anode, has been successfully achieved, in which SnO_2 nanocrystals homogenously bonded on the surfaces of 1D micro/nanosized fibers and 2D ultrathin carbon sheets, and stored inside the 3D interconnected pores. Thus, the 1D and 2D fibrous carbon matrixes were expected to be deformable under the stress resulted from volume change of SnO_2 during charge/discharge cycling. There, as illustrated in **Figure 4a**, the 1D nanofibers and 2D carbon sheets could be bendable to buffer the volume change of SnO_2, while the microfibers could split to flexible nanofibers (see SEM images in **Figure 7** and **Figure S8**) to release the internal stress of SnO_2 layer, avoiding its serious disintegration. We have also examined the fibrous carbon in a hybrid electrode during SnO_2 lithiation using *in*-situ Raman spectroscopy performed on a cell with a quartz window. **Figure 4b** shows a series of Raman spectra of SnO_2@CFP electrode collected at different potentials during the first cycle. Clearly, the SnO_2 bands disappeared when it was discharged to 0.5V, accompanyed by an obvious increase in I_D/I_G from 0.81 to 1.18 (**Figure 4d**). As mentioned earlier, a higher value of D/G band intensity ratio reflects more microstructure defects in the carbon. Thus, an increase in I_D/I_G may be attributed to more edge distortions and new surface formation in the carbon matrix due mainly to local deformation of fibrous carbon in the hybrid electrode[44]. Most notably, as seen in **Figure 4b**, the G band of carbon disappeared (and dramatically red-shifted) when the hybrid electrode was discharged to 0.01V, leaving only one broader band centered around 1400 cm^{-1}. The essential spectral features remained the same even after the hybrid electrode was recharged to 0.4V. However, as more Li^+ ions were extracted from the electrode so that the potential recharged 2.0V, the G band was nearly restored and the I_D/I_G ratio changed to 1.30 (**Figure 4d**), suggesting that there is a large, partially-reversible structure deformation in the fibrous carbon of the hybrid electrode during Li^+ insertion and extraction. The structural deformation is induced by the large volume change associated with the conversion reaction (between SnO_2

and Li_2O) and the Li-Sn alloying/de-alloying reaction in the SnO_2@CFP hybrid electrode. The structural deformation is not induced by lithium insertion into in the fibrous carbon in the CFP frame, as corroborated by the in situ Raman study of a CFP sample under the identical conditions (**Figure 4c** and **d**). In contrast, the variations in the I_D/I_G ratio at different lithiation states are relatively small, as seen from the Raman spectra shown in **Figure 4c**; this is consistent with studies of other pure carbon anode materials[44, 46]. These results confirmed that lithiation of SnO_2 actually leaded to sever deformation in the multidimensional carbon scaffolds, which could in turn effectively release the stress and prevent the pulverization of SnO_2 layers. Thus, the hybrid anode supported by multidimensional carbon scaffolds showed excellent performance.

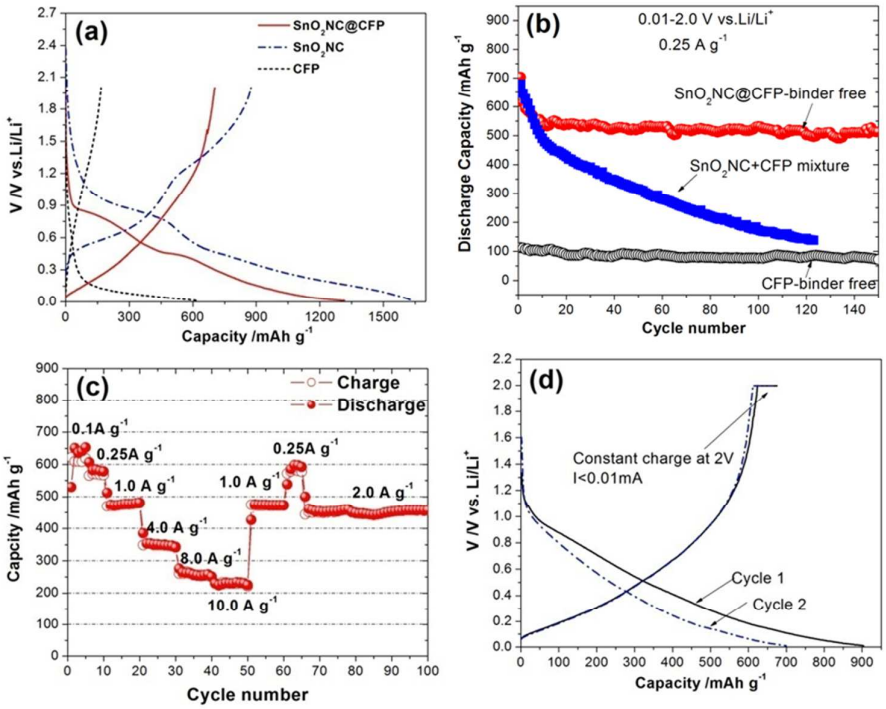

Figure 5 (a) The first-cycle charge–discharge curves for the slurry-coating pure SnO_2NC, binder-free CFP and SnO_2NC@CFP electrodes; (b) discharge capacity vs. cycle number of CFP, the slurry-coating SnO_2NC+CFP mixture, SnO_2NC@CFP electrodes cycling between 0.01 and 2V at current rate of $0.25Ag^{-1}$; (c) rate capability of SnO_2NC@CFP hybrid after cycling 150times shown in (b); (d) the first and second discharge-charge curves of the SnO_2NC@CFP after prelithiation treatment and then cycling with constant-potential charging (at 2V, until I<0.02mA).

Figure 5a shows the first charge–discharge cycle curves for the binder-free SnO_2NC@CFP anodes at current rate of 0.25Ag^{-1} between 0.01 and 2V vs. Li/Li$^+$, together with those of the pure SnO_2NC and CFP electrodes for comparison. It could be observed that there were similar plateau regions for lithiation of SnO_2 in the discharge profiles of the SnO_2NC and SnO_2NC@CFP. The SnO_2NC@CFP sheet (1cm^2) delivered an initial discharge capacity of 1,316 mAhg^{-1} with initial coulombic efficiency (CE) of 53.4%, which was near to that (53.3%) of the slurry-coating SnO_2NC electrode. The initial irreversible capacity of SnO_2NC@CFP was ~613 mAhg^{-1}, while most of them should be attributed to the solid electrolyte interphase (SEI) formation and especially the irreversible reactions on CFP because there was also a large initial irreversible capacity of 452 mAhg^{-1} in the pure CFP sheet. Nevertheless, the discharge-charge curves of the subsequent cycles (e.g., 2nd-5th, 50th, and 100th) were almost overlapped for SnO_2NC@CFP anode (Figure S6, Supporting Information), suggesting high reversibility of Li$^+$ insertion/extraction reactions in the hybrid. As recorded in **Figure 5b**, after the initial 10 cycles, the SnO_2NC@CFP electrode retained excellent capacity retention. Stable capacities of 510 mAhg^{-1} still remained after 150 cycles. Another SnO_2NC@CFP hybrid, with a lower SnO_2 content of 23wt%, could also deliver stable reversible capacities around 400 mAhg^{-1} (**Figure S7**, Supporting Information). They were much higher than those of the SnO_2NC+CFP mixture electrode with which only 160 mAhg^{-1} was retained after 120 cycles, while the CFP sheet yielded stable but very low reversible capacities (about 100mAh g^{-1}). These results suggest that the combination of SnO_2 nanocrystals with multidimensional fibrous carbon could lead to high capacity and superior cycleablitiy.

Moreover, the SnO_2NC@CFP hybrid displayed high rate capability. The electrode which had finished 150 cycles at a constant rate of 0.25Ag^{-1} (**Figure 5b**) was further cycled at varied current rates. As shown in **Figure 5c**, a reversible capacity of 652 mAh g^{-1} was obtained at the end of five charge/discharge cycles at 0.1Ag^{-1}. The capacity at 1.0Ag^{-1} was 480 mAh g^{-1},

and decreased to 230 mAh g^{-1} at a rate of 10Ag^{-1}. Surprisingly, a higher capacity (580 mAh g^{-1}) was restored when the current returned to 0.25Ag^{-1}, and a very stable capacity of 460mAh/g was yielded at a rate of 2.0Ag^{-1} after 100 cycles. The long-term cycling of the SnO_2NC@CFP anodes were repeated at high current rate of 2.0A g^{-1} (**Figure S6**, Supporting Information), also showing good cycle performance with 350 mAh^{-1} after 1000 cycles with upper limit potential at 2.0V. Here, it needs to be pointed out that, although many SnO_2-C nanocomposites could present much higher and even general increasing capacities among wide potential range of 0-3V[14, 18, 28], quite a large amount of capacities should be generated at the expense of electrolyte decomposition at high potential (from 2.0 to 3.0V). Furthermore, the capacities among potential range of 2.0-3.0V would be less meaningful for batteries using now commercial cathodes[47].

Beyond those, more attention was brought to the CE of the self-supporting SnO_2NC@CFP anode. As shown in **Figure 5d**, the initial irreversible capacity loss could be further suppressed by a prelithiation treatment[20, 48] for the hybrid and cycling with constant-potential charging (at 2V, until I <0.02mA), which leads to a higher initial CE of 74.7% and lower initial capacity loss of 229 $mAhg^{-1}$. This suggested that the initial irreversible capacity in the SnO_2NC@CFP anode was mainly attributed to the large amount of Li^+ consumed irreversibly by the defects of the carbon matrix. During prelithiation, these defects would store enough Li by diffusion and/or chemical reaction as Li foil directly contacting with the hybrid, and they would not further accept Li^+ and generate irreversible capacity loss in the electrochemical cycling afterwards. Furthermore, some Li may also react with the SnO_2NC as Li foil was in contact with hybrid, leading to less SnO_2 lithiation at the initial discharge. This is the main reason that the initial discharge-charge curves of the as-prepared electrode have different shapes from those of the electrode after pre-lithiation treatment (**Figure 5a** and **d**). The differential discharge curves also revealed that less SnO_2 reacted with Li during initial discharge in the prelithiation electrode (**Figure S8, Supporting Information**). Nevertheless,

as implied by the cyclic voltammograms, stable reactions of SnO_2 and Li were found in the SnO_2NC@CFP anode at the second and the subsequent cycles (**Figure S8**). Some SnO_2 restored after recharging to 2.0V could be also observed by *in*-situ Raman spectrum (**Figure.4b**). Thus, the reversibility of the SnO_2NC had been dramatically enhanced by loading on multidimensional fibrous carbon matrices in this hybrid.

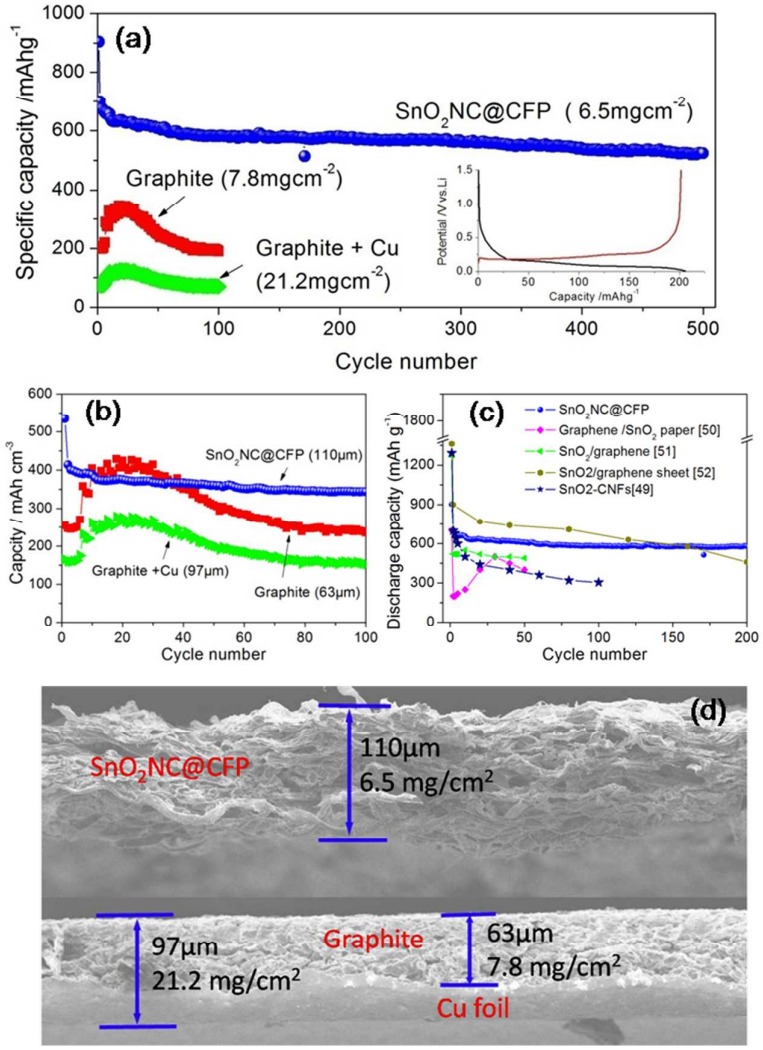

Fig.6 (**a**) Long-term cycle performance (specific capacity *vs.* cycle number) of the self-supporting SnO_2NC@CFP electrode in comparison with a commercial graphite anode coating on Cu foil. Red line is evaluated based on the mass of the graphite layer, while the green pine is based on the mass of the electrode including the Cu foil. (**b**) Comparison of the energy density of the self-supporting SnO_2NC@CFP anode with graphite anode based on the thickness of electrodes. (**c**) Comparison of cycle performance for the self-supporting SnO_2NC@CFP and other reported free-standing SnO_2-carbon fiber and SnO_2-graphene hybrid anodes. (**d**) SEM images for cross-sections of the self-supporting SnO_2NC@CFP electrode and commercial graphite anode.

Figure 6 compares long-term capacity density of a prelithiated SnO_2NC@CFP anode and a commercial graphite anode coated on Cu foil. The cross-sectional SEM images in **Figure 6d** reveal that the commercial anode consisted of a 63 μm thick graphite layer and a 34 a μm thick Cu foil. The corresponding mass is 7.8 mg cm^{-2} for the graphite layer and 21.2mg cm^{-2} for the whole electrode (graphite and Cu foil). In contrast, the self-supporting SnO_2NC@CFP anode (with a thickness of 110 μm) has a mass of 6.5 mg cm^{-2}. As shown in Figure 6a, the treated SnO_2NC@CFP anode yielded a bit higher capacities than the anode without prelithiation (**Figure 5b**). It delivered a specific capacity of 903 mAh g^{-1} in the first cycle, which was declined to 630 $mAhg^{-1}$ after the first 15 cycles. Afterward, the cycleability was excellent and the capacity slowly decreased to 526 $mAhg^{-1}$ at the 500th cycle, corresponding to a very small decay rate (*ca.* 0.03% per cycle), which is superior to that of the graphite anode. As compared in **Figure 6a**, the graphite anode has much lower specific capacities, just around 300 mAh g^{-1} (when the Cu foil is neglected) and 100 mAh g^{-1} (when the Cu foil is included). Regarding the volumetric capacity, as shown in **Figure 6c**, the self-supporting SnO_2NC@CFP anode demonstrated a stable capacity of ~400 mAh cm^{-3}, which is close to that of the graphite layer alone (when the Cu foil is neglected) but much higher than that of the entire electrode, ~200mAh cm^{-3}(when the Cu foil is included). These results indicate that the self-supporting SnO_2NC@CFP hybrid anodes have much higher capacity (both gravimetric and volumetric) than the commercial graphite anodes. It needs to be pointed out that the increasing capacities of the graphite anode during the initial cycles should be resulted from the gradually soaking of electrolyte in the coating electrode. The electrolyte could not diffuse to the inner layer of the electrode due to the absence of effective transport paths, and thus not all the graphite could react with lithium during the first several cycles. In contrast, the SnO_2@CFP hybrid could deliver stable high capacities throughout the cycling, which should be attributed to the fast transport of electrolyte and lithium ion diffusion in the 3D interconnected porous carbon matrix. Furthermore, as shown in **Figure 6d**, we also compared

the cycling performance of this SnO_2NC@CFP hybrid anode with many other free-standing SnO_2-C electrodes supported by 1D carbon nanofibers (CNFs)[49] or 2D graphene nanosheets[50-52]. Among them, the SnO_2NC@CFP anode demonstrated the best cycling stability, attributed mainly to the combination of 1D, 2D, and 3D configuration of the fibrous carbon in the CFP. In particular, the deformable carbon scaffolds and the strong bonding of ultrafine nano-size SnO_2 with carbon are the main attributes that help to effectively maintain the structure integrity of the SnO_2 during cycling.

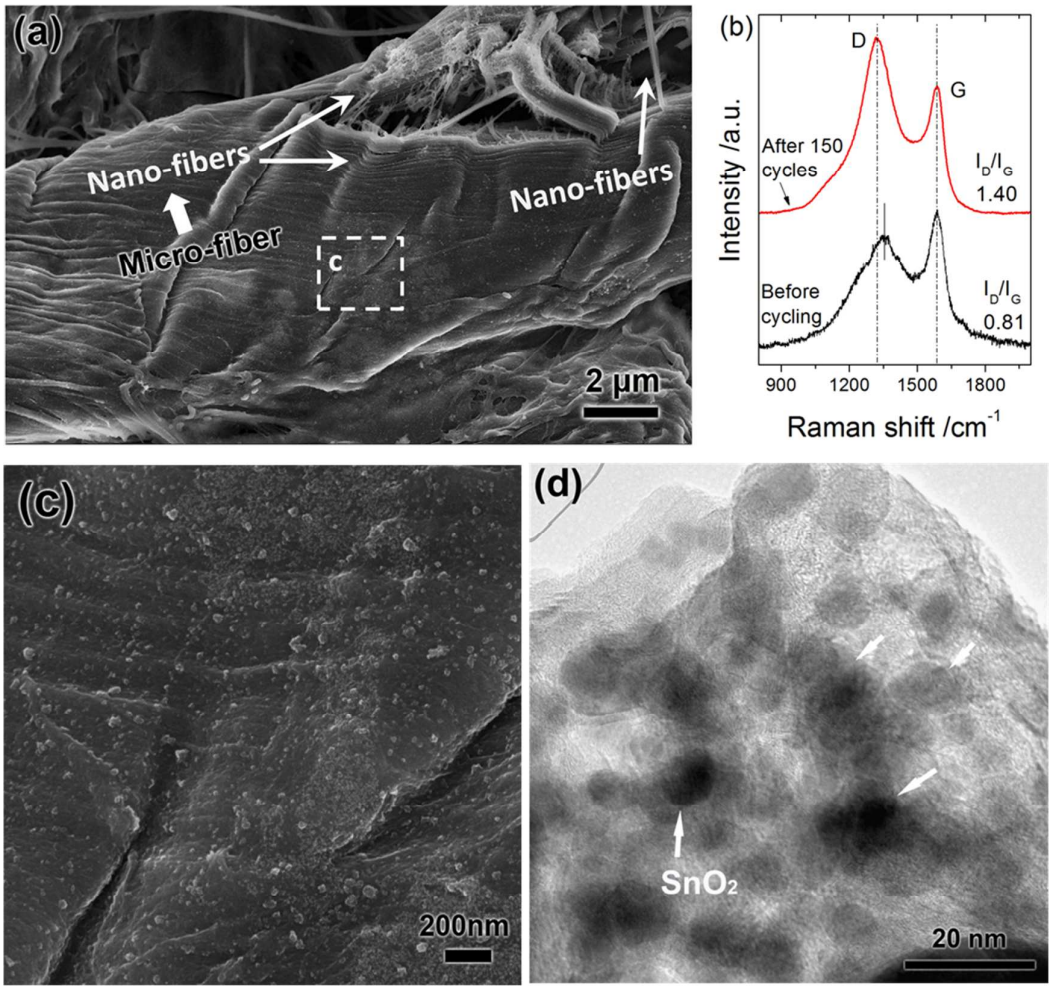

Figure 7 (a) SEM image for the binder-free SnO_2NC@CFP hybrid after150 cycles; (b) Raman shits for the carbon in the hybrid before and after 150 cycles; (c) Enlarge SEM image for the zone circled in (a); (d) TEM image for the 2D ultrathin carbon in the cycled hybrid.

The detailed microstructure variation of a SnO_2NC@CFP electrode after 150 cycles was

examined, while here the electrode was taken out from the cell and cleaned before testing. It was found that the interconnected porous structure was maintained in the hybrid sheets (**Figure S9**, Supporting Information). However, as shown in **Figure 7a**, there was obvious deformation inside the 1D microfiber scaffold, where part of the carbon had been split to form many nanofibers. Actually the split zones were very common in the microsized fibers and the ultrathin carbon sheets (**Figure S9**), which should be driven by the severe stress due to volume change of the SnO_2 layers during cycling. The structure variation of the fibrous carbon was also reflected by their Raman shifts shown in **Figure 7b**. A noticeable increase in the I_D / I_G of fibrous carbon (from 0.83 to 1.40) was also observed for hybrid after cycling 150 times. **Figure 7c** shows the enlarged SEM image for the square area in **Figure 7a**, where the active SnO_2 particles still homogeneously dispersed and tightly covered on the microfibers. TEM and HRTEM analysis, as shown in **Figure 7d** and **Figure S9** (Supporting Information), further revealed that the homogeneous distribution of SnO_2 /Sn nanocrystals in 2D ultrathin carbon sheet was maintained, without obvious increase of particle size. This suggested that the fibrous carbon effectively suppressed the aggregation of SnO_2/Sn nanoparticles during cycling, which could be responsible for the long-term cycleability of this self-supporting hybrid anode.

4. Conclusions

In summary, SnO_2 nanocrystals were deposited on carbonized filter papers to form a deformable self-supporting SnO_2NC@CFP hybrid anode. The SnO_2NC particles were homogenously accreted on the surfaces of micro/nanosized carbon fibers and ultrathin carbon sheets as well as inside the interconnected pores of the multidimensional matrices. The SnO_2NC@CFP hybrid electrode exhibited long cycling life and excellent rate capability, and superior capacity density than the commercial graphite anode, which were attributed mainly to the good dispersion of SnO_2 nanocrystals in 1D and 2D conductive carbon and the fast Li^+

transport in the 3D porous structure. In particular, the deformable fibrous carbon matrices, which facilitate stress release from the active SnO_2 during discharge-charge cycling, helped greatly to maintain good structure integrity of the SnO_2NC@CFP binder-free anode. This demonstrated that multidimensional architecture of deformable carbon matrices combining with nanoscale active materials would be a desirable approach to realize good cycle performance in high capacity Li storage materials. Furthermore, binder-free anode should also be an alternative way to achieve high energy density in batteries.

Acknowledgements

The work was supported by the National Science Foundation of China (No.51201065 and 51231003), the Doctorate Foundation of Ministry of Education (20120172120007), the Foundation for the Author of Excellent Doctoral Dissertation of Guangdong Province (SYBZZXM201309), and the Fundamental Research Funds for the Central Universities (2014ZM0002). R.Z.Hu was supported by China Scholarship Council (201406155009).

Supporting Information

Supporting Information is available online or from the author.

Reference

[1] V. Etacheri, R. Marom, R. Elazari, G. Salitra, D. Aurbach, Energy & Environmental Science, 4 (2011) 3243-3262.
[2] M.G. Kim, J. Cho, Advanced Functional Materials, 19 (2009) 1497-1514.
[3] P.A. Connor, J.T.S. Irvine, Journal of Power Sources, 97-98 (2001) 223-225.
[4] L. Yuan, K. Konstantinov, G.X. Wang, H.K. Liu, S.X. Dou, Journal of Power Sources, 146 (2005) 180-184.
[5] J.Y. Huang, L. Zhong, C.M. Wang, J.P. Sullivan, W. Xu, L.Q. Zhang, S.X. Mao, N.S. Hudak, X.H. Liu, A. Subramanian, H. Fan, L. Qi, A. Kushima, J. Li, Science, 330 (2010) 1515-1520.
[6] Y. Idota, T. Kubota, A. Matsufuji, Y. Maekawa, T. Miyasaka, Science, 276 (1997) 1395-1397.
[7] A. Nie, L.-Y. Gan, Y. Cheng, H. Asayesh-Ardakani, Q. Li, C. Dong, R. Tao, F. Mashayek, H.-T. Wang, U. Schwingenschlögl, R.F. Klie, R.S. Yassar, ACS Nano, 7 (2013) 6203-6211.
[8] P. Meduri, C. Pendyala, V. Kumar, G.U. Sumanasekera, M.K. Sunkara, Nano Letters, 9 (2009) 612-616.
[9] X.W. Lou, Y. Wang, C. Yuan, J.Y. Lee, L.A. Archer, Advanced Materials, 18 (2006) 2325-2329.

[10] Y. Wang, H.C. Zeng, J.Y. Lee, Advanced Materials, 18 (2006) 645-649.
[11] R. Retoux, T. Brousse, D.M. Schleich, Journal of The Electrochemical Society, 146 (1999) 2472-2476.
[12] C. Kim, M. Noh, M. Choi, J. Cho, B. Park, Chemistry of Materials, 17 (2005) 3297-3301.
[13] T. Brousse, R. Retoux, U. Herterich, D.M. Schleich, Journal of The Electrochemical Society, 145 (1998) 1-4.
[14] X. Li, X. Meng, J. Liu, D. Geng, Y. Zhang, M.N. Banis, Y. Li, J. Yang, R. Li, X. Sun, M. Cai, M.W. Verbrugge, Advanced Functional Materials, 22 (2012) 1647-1654.
[15] X. Li, A. Dhanabalan, L. Gu, C. Wang, Advanced Energy Materials, 2 (2012) 238-244.
[16] S. Ding, J.S. Chen, X.W. Lou, Advanced Functional Materials, 21 (2011) 4120-4125.
[17] G. Chen, Z. Wang, D. Xia, Chemistry of Materials, 20 (2008) 6951-6956.
[18] D. Wang, J. Yang, X. Li, D. Geng, R. Li, M. Cai, T.-K. Sham, X. Sun, Energy & Environmental Science, 6 (2013) 2900-2906.
[19] L. Zhang, H.B. Wu, B. Liu, X.W. Lou, Energy & Environmental Science, 7 (2014) 1013-1017.
[20] R. Hu, W. Sun, H. Liu, M. Zeng, M. Zhu, Nanoscale, 5 (2013) 11971-11979.
[21] J. Liang, X.-Y. Yu, H. Zhou, H.B. Wu, S. Ding, X.W. Lou, Angewandte Chemie International Edition, 53 (2014) 12803-12807.
[22] J.S. Chen, X.W. Lou, Small, 9 (2013) 1877-1893.
[23] X.W. Lou, C.M. Li, L.A. Archer, Advanced Materials, 21 (2009) 2536-2539.
[24] J.S. Chen, Y.L. Cheah, Y.T. Chen, N. Jayaprakash, S. Madhavi, Y.H. Yang, X.W. Lou, The Journal of Physical Chemistry C, 113 (2009) 20504-20508.
[25] M.-S. Park, Y.-M. Kang, G.-X. Wang, S.-X. Dou, H.-K. Liu, Advanced Functional Materials, 18 (2008) 455-461.
[26] J. Wang, W. Li, F. Wang, Y. Xia, A.M. Asiri, D. Zhao, Nanoscale, 6 (2014) 3217-3222.
[27] F. Ye, B. Zhao, R. Ran, Z. Shao, Chemistry – A European Journal, 20 (2014) 4055-4063.
[28] X. Zhou, L.-J. Wan, Y.-G. Guo, Advanced Materials, 25 (2013) 2152-2157.
[29] Y. Wang, D. Su, C. Wang, G. Wang, Electrochemistry Communications, 29 (2013) 8-11.
[30] S. Yang, H. Song, H. Yi, W. Liu, H. Zhang, X. Chen, Electrochimica Acta, 55 (2009) 521-527.
[31] Z. Wang, G. Chen, D. Xia, Journal of Power Sources, 184 (2008) 432-436.
[32] Q. Guo, Z. Zheng, H. Gao, J. Ma, X. Qin, Journal of Power Sources, 240 (2013) 149-154.
[33] J. Cheng, H. Xin, H. Zheng, B. Wang, Journal of Power Sources, 232 (2013) 152-158.
[34] Y. Li, X. Lv, J. Lu, J. Li, The Journal of Physical Chemistry C, 114 (2010) 21770-21774.
[35] Y. Su, S. Li, D. Wu, F. Zhang, H. Liang, P. Gao, C. Cheng, X. Feng, ACS Nano, 6 (2012) 8349-8356.
[36] P. Gurunathan, P.M. Ette, K. Ramesha, ACS Applied Materials & Interfaces, 6 (2014) 16556-16564.
[37] A. Jahel, C.M. Ghimbeu, L. Monconduit, C. Vix-Guterl, Advanced Energy Materials, 4 (2014) 10.1002/aenm.201400025.
[38] Y. Yu, C.H. Chen, Y. Shi, Advanced Materials, 19 (2007) 993-997.
[39] Z. Chen, M. Zhou, Y. Cao, X. Ai, H. Yang, J. Liu, Advanced Energy Materials, 2 (2012) 95-102.
[40] R. Hu, M. Zhu, H. Wang, J. Liu, O. Liuzhang, J. Zou, Acta Materialia, 60 (2012) 4695-4703.
[41] W. Xia, Y. Wang, Y. Luo, J. Li, Y. Fang, L. Gu, J. Peng, J. Sha, Journal of Power Sources, 217 (2012) 351-357.
[42] B. Zhao, G. Yang, R. Ran, C. Kwak, D.W. Jung, H.J. Park, Z. Shao, Journal of Materials Chemistry A, 2 (2014) 9126-9133.
[43] X. Liu, Y. Gu, J. Huang, Chemistry – A European Journal, 16 (2010) 7730-7740.
[44] R. Baddour-Hadjean, J.-P. Pereira-Ramos, Chemical Reviews, 110 (2009) 1278-1319.

[45] E. Fazio, F. Neri, S. Savasta, S. Spadaro, S. Trusso, Physical Review B, 85 (2012) 195423.
[46] L.J. Hardwick, P.W. Ruch, M. Hahn, W. Scheifele, R. Kötz, P. Novák, Journal of Physics and Chemistry of Solids, 69 (2008) 1232-1237.
[47] A. Kraytsberg, Y. Ein-Eli, Advanced Energy Materials, 2 (2012) 922-939.
[48] N. Liu, L. Hu, M.T. McDowell, A. Jackson, Y. Cui, ACS Nano, 5 (2011) 6487-6493.
[49] D. Kim, D. Lee, J. Kim, J. Moon, ACS Applied Materials & Interfaces, 4 (2012) 5408-5415.
[50] J. Liang, Y. Zhao, L. Guo, L. Li, ACS Applied Materials & Interfaces, 4 (2012) 5742-5748.
[51] S. Jiang, B. Zhao, R. Ran, R. Cai, M.O. Tade, Z. Shao, RSC Advances, 4 (2014) 9367-9371.
[52] S. Liu, R. Wang, M. Liu, J. Luo, X. Jin, J. Sun, L. Gao, Journal of Materials Chemistry A, 2 (2014) 4598-4604.

Graphical Abstract

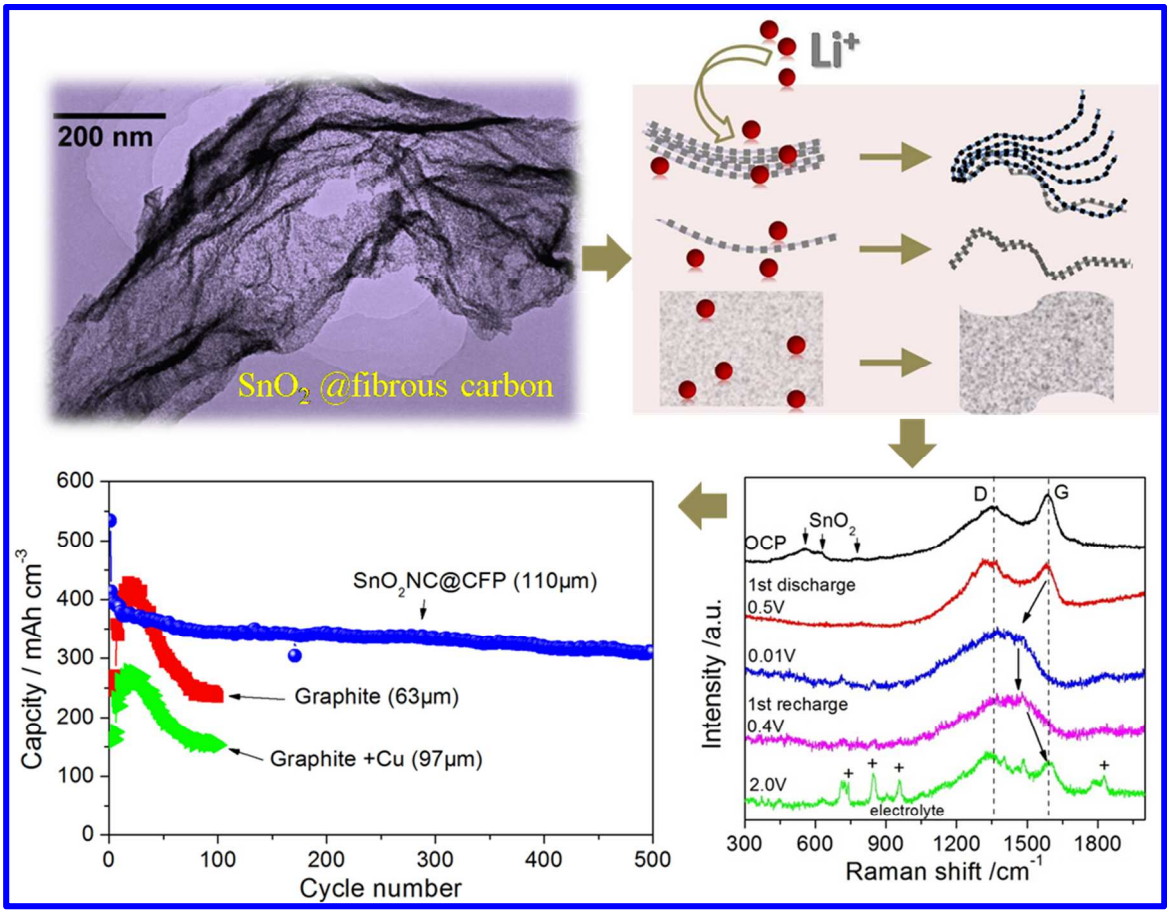

A free-standing hybrid anode for Li-ion battery was fabricated by filling ultrafine SnO_2 nanocrystals (NC) into multidimensional fibrous carbon derived from carbonized filter paper (CFP). The SnO_2NC@CFP hybrid anode demonstrated excellent rate capability and long cycling life, which are attributed, respectively, to the high dispersion state of SnO_2 NC and the deformable fibrous carbon scaffolds flexible to release the stress from the SnO_2 during cycling.